Incorporation of polar Mellin transform in a hybrid optoelectronic correlator for scale and rotation invariant target recognition

Mehjabin Sultana Monjur,[1,*] Shih Tseng,[1,4] Renu Tripathi,[3] and M. S. Shahriar[1,2]

[1]*Department of Electrical Engineering and Computer Science, Northwestern University, Evanston, Illinois 60208, USA*
[2]*Department of Physics and Astronomy, Northwestern University, Evanston, Illinois 60208, USA*
[3]*OSCAR, Department of Physics and Engineering, Delaware State University, Dover, Delaware 19901, USA*
[4]*Digital Optics Technologies, Rolling Meadows, Illinois 60008, USA*
**Corresponding author: mehjabin@u.northwestern.edu*

Received February 12, 2014; revised April 15, 2014; accepted April 16, 2014;
posted April 17, 2014 (Doc. ID 206271); published May 16, 2014

In this paper, we show that our proposed hybrid optoelectronic correlator (HOC), which correlates images using spatial light modulators (SLMs), detectors, and field-programmable gate arrays (FPGAs), is capable of detecting objects in a scale and rotation invariant manner, along with the shift invariance feature, by incorporating polar Mellin transform (PMT). For realistic images, we cut out a small circle at the center of the Fourier transform domain, as required for PMT, and illustrate how this process corresponds to correlating images with real and imaginary parts. Furthermore, we show how to carry out shift, rotation, and scale invariant detection of multiple matching objects simultaneously, a process previously thought to be incompatible with PMT-based correlators. We present results of numerical simulations to validate the concepts. © 2014 Optical Society of America

OCIS codes: (070.0070) Fourier optics and signal processing; (100.0100) Image processing; (130.0130) Integrated optics; (070.4550) Correlators; (100.3005) Image recognition devices; (130.0250) Optoelectronics.
http://dx.doi.org/10.1364/JOSAA.31.001259

1. INTRODUCTION

Target identification and tracking is important in many defense and civilian applications. Optical correlators provide a simple technique for fast verification and identification of data. The simplest form of such a device is the basic Vander Lugt [1–3] optical correlator. The limitation of this correlator is that the recording process is time consuming. This constraint is circumvented in a joint transform correlator (JTC) [4–7], where a dynamic material such as photorefractive polymer film is used so that the recording and correlation take place simultaneously. A JTC of this type suffers from many practical problems and constraints. As an alternative, we recently proposed a hybrid optoelectronic correlator (HOC) [8] where the nonlinearity provided by the JTC medium is replaced by the nonlinearity of high-speed detectors. The advantage of this approach as compared to previous architecture that also employs detectors [9] has been discussed in detail in [8]. As shown in [8], the HOC is capable of shift-invariant image recognition, in the same manner as what is achieved with a conventional holographic correlator (CHC). However, the actual architecture is very different, requiring many intermediate steps, servos, and postprocessing. Furthermore, the output signals are also different (e.g., it contains a cross-correlation term and an anti-cross-correlation term, but no convolution nor dc term). Thus it may not be *a priori* obvious whether the HOC can also perform scale and rotation invariant correlation using polar Mellin transform (PMT) [10–17].

In this paper, we show how it is possible to use PMT to achieve scale and rotation invariant image recognition with the HOC architecture. Furthermore, we identify some limitations of using PMT in the CHC architecture proposed previously, and we show how to overcome these constraints by proper preprocessing of images for both CHC and HOC.

The paper is organized as follows: Section 2 describes the proposed HOC architecture incorporating PMT to achieve scale and rotation invariance in addition to shift invariance. Section 3 presents a brief review of the underlying concepts of PMT for achieving scale and rotation invariance. Section 4 illustrates the simulation results using MATLAB, which shows that the proposed system is capable of detecting an image in a scale and rotation invariant manner. In this section, we also point out some limitations of using PMT in the CHC architecture as proposed previously and show how to overcome these constraints. Section 5 describes the process of detecting multiple objects in a shift, scale, and rotation invariant manner using the HOC architecture and show the simulation results. The paper concludes with a summary and outlook in section 6.

2. PROPOSED HYBRID OPTOELECTRONIC CORRELATOR INCORPORATING PMT

The details of the HOC proposed by us can be found in [8]. Briefly, in the shift invariant HOC architecture, the Fourier transform (FT) of the reference image is interfered with a plane wave, and the resulting signal is recorded with a detector array. Similarly, the FT of the object image is also interfered with a plane wave, and the resulting signal is recorded with another detector array. These signals are then processed in a certain manner, as described below, and then sent to an SLM to perform the correlation in the optical domain.

 © 2014 Optical Society of America

Figure 1 shows an overview of the HOC architecture, which can be used to correlate two images, R_j and Q_j. Here, R_j and Q_j can each be a conventional image or the PMT processed version of a conventional image. The process for producing a PMT processed version of a conventional image will be described later in this section. We envision a scenario, where a set of reference images, R_j, are stored in a database. A particular image of interest is then retrieved from the database for correlation. If a digital database (such as computer hard drive) is used, then the image is converted to the optical domain using an SLM. The optical image (R_j) is Fourier transformed by a lens. It is then split into two identical ports, both designated as M_r. In one port, the image is detected by an array of detectors, which could be a high-resolution focal plane array (FPA) or a digital CMOS camera. The signal array produced by the camera is denoted as B_r. The camera is interfaced with a field programmable gate array (FPGA) via a USB cable. B_r can be stored in the built-in memory of the FPGA [FPGA-1]. In the other port, M_r is interfered with a plane wave C_r, and detected with another CMOS camera, producing the digital signal array A_r and is stored in the memory of FPGA-1. A_r and B_r can be expressed as

$$A_r = |M_r e^{j\phi_r} + C_r e^{j\psi_r}|^2 = |M_r|^2 + |C_r|^2 + |M_r||C_r|e^{j(\phi_r-\psi_r)} + |M_r||C_r|e^{-j(\phi_r-\psi_r)}, \tag{1}$$

$$B_r = |M_r|^2. \tag{2}$$

In addition, the intensity profile of the plane wave ($|C_r|^2$) is measured, by blocking the image path momentarily, using a shutter (not shown), and the information is stored in the memory component of FPGA-1. FPGA-1 then computes and stores S_r, which can be expressed as

$$S_r = A_r - B_r - |C_r|^2 = M_r C_r^* + M_r^* C_r = |M_r||C_r|e^{j(\phi_r-\psi_r)} + |M_r||C_r|e^{-j(\phi_r-\psi_r)}. \tag{3}$$

Here, ϕ_r is the phase of the Fourier transformed image, M_r, and Ψ_r is the phase of the plane wave, C_r. It should be noted that ϕ is a function of (x, y), assuming that the image is in the (x, y) plane. This subtraction process has to be done pixel by pixel using one or more subtractors available in the FPGA.

The captured query image is also transferred to the optical domain using another SLM (SLM-2) to form Q_j. The optical image (Q_j) is Fourier transformed by a lens and is split into two identical ports, both designated as M_q. In a manner similar to what is described above for the reference image, the signal $S_q = A_q - B_q - |C_q|^2$ is produced using two cameras and an FPGA (FPGA-2) and stored in FPGA-2 memory. Here, C_q is the amplitude of an interfering plane wave, and the other quantities are given as follows:

$$A_q = |M_q + C_q|^2 = |M_q|^2 + |C_q|^2 + |M_q||C_q|e^{j(\phi_q-\psi_q)} + |M_q||C_q|e^{-j(\phi_q-\psi_q)}, \tag{4}$$

$$B_q = |M_q|^2, \tag{5}$$

$$S_q = A_q - B_q - |C_q|^2 = M_q C_q^* + M_q^* C_q = |M_q||C_q|e^{j(\phi_q-\psi_q)} + |M_q||C_q|e^{-j(\phi_q-\psi_q)}. \tag{6}$$

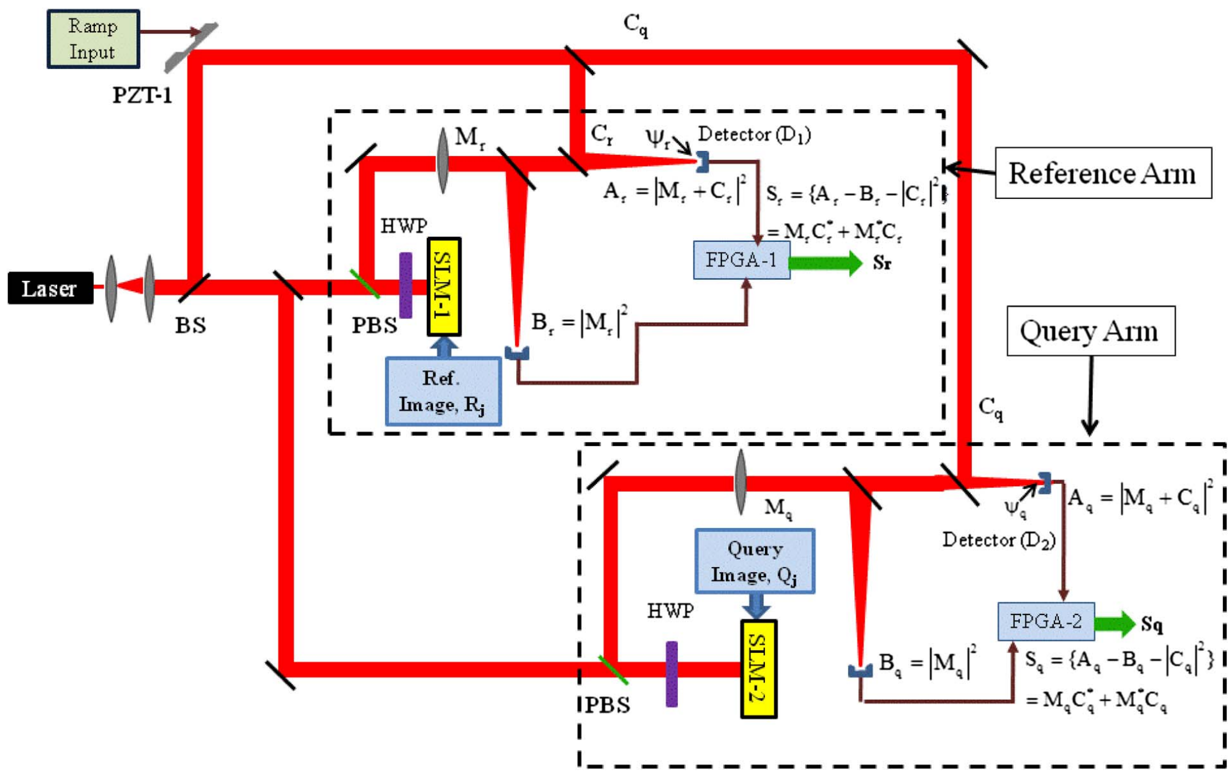

Fig. 1. Illustration of the architecture of an HOC. PMT, polar Mellin transform; PBS, polarizing beam splitter; BS, beam splitter; HWP, half-wave plate; PZT, piezoelectric transducer.

As before, $\phi_q(x,y)$ is the phase of the Fourier-transformed image, M_q, and Ψ_q is the phase of the plane wave C_q.

In the final stage of the hybrid correlator (as shown in Fig. 2), these two signals (S_r and S_q) described in Eqs. (3) and (6) are multiplied together using the multiplier in FPGA-3. Four-quadrant multiplication can easily be implemented using an FPGA. The resulting signal array, S, is stored in FPGA-3 memory. This can be expressed as

$$\begin{aligned} S = S_r \cdot S_q &= (M_r C_r^* + M_r^* C_r) \cdot (M_q C_q^* + M_q^* C_q) \\ &= [\alpha^* M_r M_q + \alpha M_r^* M_q^* + \beta^* M_r M_q^* + \beta M_r^* M_q], \end{aligned} \tag{7}$$

where $\alpha \equiv |C_r||C_q|e^{j(\Psi_r+\Psi_q)}$; $\beta \equiv |C_r||C_q|e^{j(\Psi_r-\Psi_q)}$.

This signal array, S, is now transferred to another SLM (SLM-3) from FPGA-3 through the digital visual interface (DVI) port. Since S can be positive or negative, the SLM should be operated in a bipolar amplitude mode. The optical image produced by SLM-3 is Fourier transformed using a lens, producing the signal S_f, given by

$$\begin{aligned} S_f = \alpha^* F(M_r M_q) + \alpha F(M_r^* M_q^*) + \beta^* F(M_r M_q^*) \\ + \beta F(M_r^* M_q). \end{aligned} \tag{8}$$

Here, F stands for the FT. Since M_α ($\alpha = r$ or q) is the FT of the images R_j or Q_j, using the well-known relations between the FT of products of functions, and convolutions and cross-correlations, we can express the final signal as the sum of four terms:

$$\begin{aligned} S_f &= \alpha^* T_1 + \alpha T_2 + \beta^* T_3 + \beta T_4, \\ T_1 &= R_j(x,y) \otimes Q_j(x,y), \\ T_2 &= R_j^*(-x,-y) \otimes Q_j^*(-x,-y), \\ T_3 &= R_j(x,y) \odot Q_j(x,y), \\ T_4 &= Q_j(x,y) \odot R_j(x,y), \end{aligned} \tag{9}$$

where $\otimes$ indicates 2D convolution, and $\odot$ indicates 2D cross-correlation. We can now make the following observations:

- T_1 represents the 2D convolution of the images, R_j and Q_j.
- T_2 represents the 2D convolution of the images, R_j and Q_j, but with each conjugated and inverted along both axes.
- T_3 represents the 2D cross correlation of the images, R_j and Q_j.
- T_4 represents the 2D cross correlation of the images, Q_j and R_j. (Cross correlation is noncommutative; hence, T_3 is not necessarily equal to T_4). We denote it as the anticross-correlation signal.

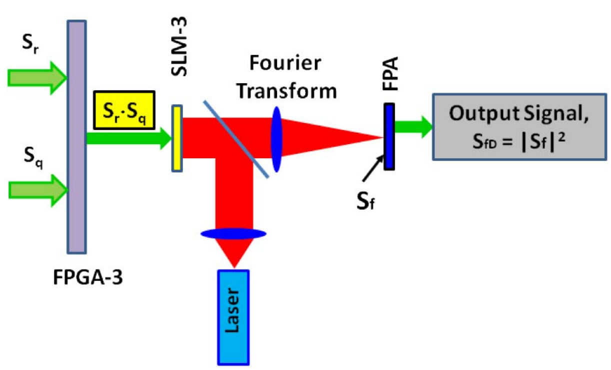

Fig. 2. Final stage of the HOC.

The cross-correlation technique is usually used to find matches between two objects. In our architecture, we have convolution terms (T_1 and T_2) in addition to cross-correlation terms (T_3 and T_4). The convolution terms can be washed out by implementing a phase stabilization and scanning technique in the HOC architecture, which has been discussed in detail in [8].

The CHC [2–4] has one convolution term and one cross-correlation term, along with some dc and low spatial frequency outputs. In contrast, the HOC architecture, after incorporating the phase stabilization and scanning, has only two outputs: a cross-correlation (T_3) and an anti-cross-correlation term (T_4). The strengths of T_3 and T_4 are the same, and they appear as symmetric signals in the presence of a shift. This difference has to be kept in mind in using the HOC architecture.

The signal observed by the final FPA, is, of course, given by $S_{fD} \equiv \alpha |S_f|^2$, where α is a proportionality constant, which we set to be unity for simplicity of discussion. Thus, assuming that the contributions from T_1 and T_2 are eliminated via the combination of phase scanning and low-pass filtering [8], the final FPA signal can be expressed as

$$S_{fD} = |\beta^* T_3 + \beta T_4|^2 = |\beta^* F(M_r M_q^*) + \beta F(M_r^* M_q)|^2. \tag{10}$$

It is useful to consider two different scenarios in order to interpret the information one can glean from this signal.

Scenario 1: Perfectly Matched Images with no Relative Shift

In this case, $T_3 = T_4$, so that Eq. (10) can be expressed as $S_{fD} = |\beta^* + \beta|^2 |T_3|^2 = 4|\beta|^2 \cos^2(\Psi_r - \Psi_q)|T_3|^2$. This signal is maximum when $(\Psi_r - \Psi_q) = 0$. As discussed in [8], this situation (i.e., use of identical, unshifted images) thus can be used to keep the servo locked to the position, where $(\Psi_r - \Psi_q) = 0$. Thus we will assume from now on that $(\Psi_r - \Psi_q) = 0$, so that $\beta = \beta^* = |\beta|$.

Scenario 2: Perfectly Matched Images with a Relative Shift in Position

If the query image is shifted by a vector $\vec{\rho}_0$, then $M_q = M_r \exp(j2\pi\vec{f}\cdot\vec{\rho}_0)$. Hence we can write: $M_r M_q^* = |M_r|^2 \exp(-j2\pi\vec{f}\cdot\vec{\rho}_0)$; $M_r^* M_q = |M_r|^2 \exp(j2\pi\vec{f}\cdot\vec{\rho}_0)$. Now we define $F(|M_r|^2) \equiv G_0(\vec{\rho}_0)$, where F stands for FT. It then follows that $T_3 = F(M_r M_q^*) = F(|M_r|^2 \exp(-j2\pi\vec{f}\cdot\vec{\rho}_0)) = G_0(\vec{\rho} - \vec{\rho}_0)$. Similarly, $T_4 = F(M_r^* M_q) = F(|M_r|^2 \exp(j2\pi\vec{f}\cdot\vec{\rho}_0)) = G_0(\vec{\rho} + \vec{\rho}_0)$. The spatial extent of $G_0(\vec{\rho})$ is determined by the size of the image. Let us quantify this by defining a radial extent, $|\vec{\rho}_m|$ such that $G_0(\vec{\rho}) = 0$ for $|\vec{\rho}| \geq |\vec{\rho}_m|$. The behavior of the final signal depends on the value of the parameter, $\eta \equiv |\vec{\rho}_0|/|\vec{\rho}_m|$.

Case I: Consider first the situation, where $\eta \geq 1$. In this case, there is no overlap between $G_0(\vec{\rho} - \vec{\rho}_0)$ and $G_0(\vec{\rho} + \vec{\rho}_0)$ (i.e., between T_3 and T_4). Thus the final detector signal of Eq. (10) can be expressed as $S_{fD} = |\beta|^2(|T_3|^2 + |T_4|^2)$. In this case, we will see two distinct peaks, corresponding to the cross-correlation (T_3) and anti-cross-correlation (T_4). We would like to point out that, for the sake of simplicity, this condition was implicitly assumed to hold in the discussions presented in [8].

Case II: Consider next the situation, where $\eta < 1$. In this case, the final detector signal can be expressed as $S_{fD} = |\beta|^2 |G_0(\vec{\rho} - \vec{\rho}_0) + G_0(\vec{\rho} + \vec{\rho}_0)|^2 = |\beta|^2 |T_3 + T_4|^2$. The shape of this signal depends on the details of the images and thereby on the details of T_3 and T_4. In what follows, we illustrate the shape of the signal S_{fD} for both Case I and II, with a few examples.

For clarity, we consider first examples of 1D images. Figures 3(a) and 3(b) show two images, with Gaussian profiles, shifted from each other by $|\vec{\rho}_0| = 4\sigma$, where $\sigma = 5$ mm is the half-width of each image. Here, a reasonable estimate for $|\vec{\rho}_m|$ is 3σ, so that $\eta > 1$ is satisfied, corresponding to Case I. As can be seen in Fig. 3(c), the signal now has two distinct peaks. Next we consider again the same images, but with a smaller shift: $|\vec{\rho}_0| = 2\sigma$, shown in Figs. 3(d) and 3(e). In this case, $\eta = 0.67$, corresponding to Case II, so that there will be overlaps between T_3 and T_4. However, the two peaks can still be discerned in the final signal, shown in Fig. 3(f). Finally, we consider a case where $|\vec{\rho}_0| = \sigma$, as shown in Figs. 3(g) and 3(h). In this case, $\eta = 0.25$, and we can see that the peaks are no longer distinguishable and have merged into each other, as shown in Fig 3(i).

Next we consider some examples in two dimensions. Figures 4(a) and 4(b) show two identical images, shifted from each other by $|\vec{\rho}_0| \approx 0.02$ m. For this image $|\vec{\rho}_m| \approx 0.01$ m, so that $\eta > 1$ is satisfied, corresponding to Case I. As can be seen in Fig. 4(c), the signal now has two distinct sharp peaks.

Next we consider again the same images, but with a smaller shift: $|\vec{\rho}_0| \approx 0.004$ m, shown in Figs. 4(d) and 4(e). In this case $\eta \approx 0.4$, corresponding to case II, so that there will be overlaps between T_3 and T_4. However, the two peaks can still be discerned in the final signal, shown in Fig. 4(f). Finally, we consider a case, where $|\vec{\rho}_0| \approx 0.001$ m, as shown in Figs. 4(g) and 4(h). In this case, $\eta \approx 0.09$, and we can see that the peaks are no longer distinguishable and have merged into each other, as shown in Fig 4(i).

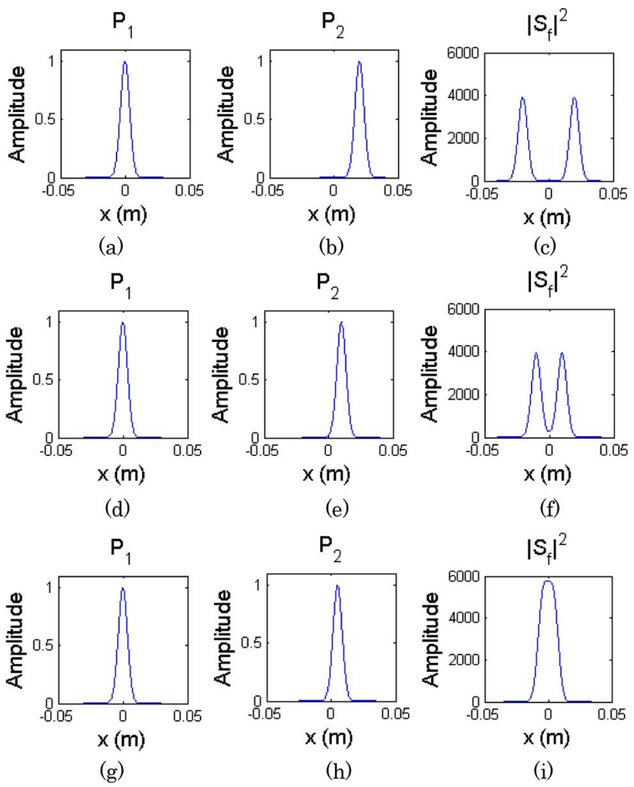

Fig. 3. Illustration of the resolving power of the HOC architecture for 1D identical images.

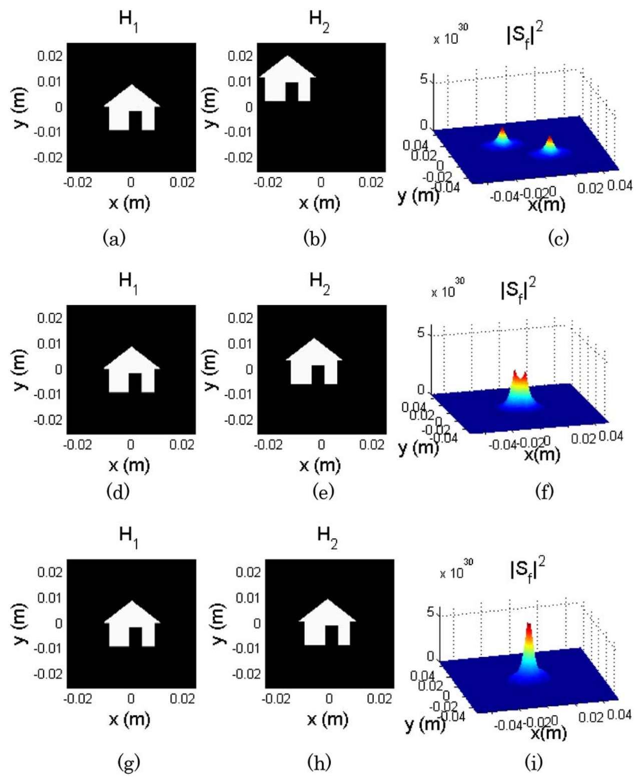

Fig. 4. Illustration of the resolving power of the HOC architecture for 2D identical images.

If the cross-correlation peaks are clearly resolved, then we can infer the distance between the two matched images, given by half the separation between the peaks. However, this information cannot be retrieved when the peaks are not resolved. On the other hand, the ability of the HOC architecture to determine whether a match is found is not adversely affected by the potential overlap between T_3 and T_4. Additional implications of this potential overlap between T_3 and T_4 are addressed in other sections of this paper. Note that in other sections of the paper, we will assume that the convolution terms (T_1 and T_2) have been eliminated by the phase stabilization and scanning circuit.

A. Incorporating Polar Mellin Transform in the HOC Architecture

If we start with regular reference and query images for the HOC architecture described above, it can detect images in shift invariant manner only. The architecture can be extended to achieve scale and rotation invariance, along with shift invariance, by transforming the reference and query images to log-polar domain. The flow diagram of performing this transformation, which is generally called the PMT, is described in Fig. 5(a), and the detailed architecture is described in Fig. 5(b). We start with an image $U(x', y')$ [query or reference image and converted to optical domain using an SLM as shown in Fig. 5(b)]. The coordinates have dimensions of distance, e.g., meter. The next step is to find the FT of the image, $\tilde{U}(k'_x, k'_y)$, where the coordinates have dimensions of per meter. For notational convenience, we redefine $k'_x \to x$

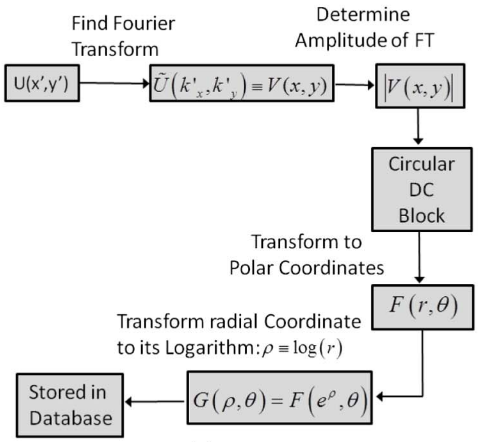

(a)

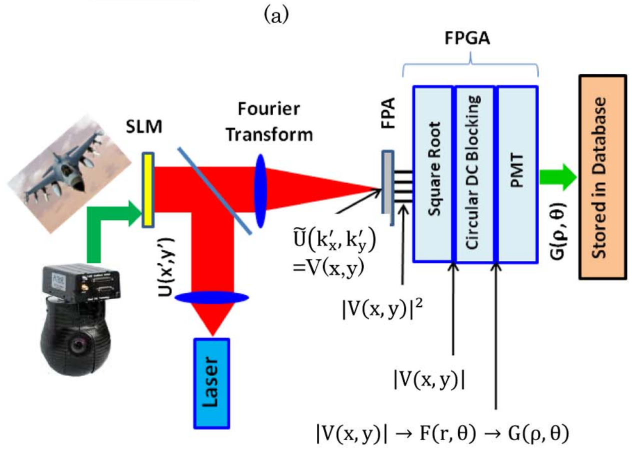

(b)

Fig. 5. (a) Flow diagram for transforming of query/reference image to the log-polar domain. (b) Schematic illustration of the architecture for implementing PMT.

and $\mathrm{k}'_y \rightarrow \mathrm{y}$, and denote as $\mathrm{V}(\mathrm{x},\mathrm{y})$ to be the same as $\tilde{\mathrm{U}}(\mathrm{k}'_x, \mathrm{k}'_y)$. In practice, the original image, $\mathrm{U}(\mathrm{x}', \mathrm{y}')$ would be represented in the optical domain by using an SLM linked to a camera or a computer database. A lens would be used to find the FT: $\tilde{\mathrm{U}}(\mathrm{k}'_x, \mathrm{k}'_y) \equiv \mathrm{V}(\mathrm{x},\mathrm{y})$. An FPA detects the intensity of the Fourier transformed image, i.e., $|\mathrm{V}(\mathrm{x},\mathrm{y})|^2$. The FPA is interfaced with the FPGA, which determines the value of $|\mathrm{V}(\mathrm{x},\mathrm{y})|$, thus eliminating the phase information. The magnitude of the FT of an object or function is invariant to a shift in the function $|\mathrm{F}\{\mathrm{f}(\mathrm{x},\mathrm{y})\}| = |\mathrm{F}\{\mathrm{f}(\mathrm{x} - \mathrm{x}_0)\}|$, but not to a scale change in the input. A circular hole of small radius (e.g., radius of five units) on $|\mathrm{V}(\mathrm{x},\mathrm{y})|$ is created using the FPGA. The necessity of creating this hole is discussed in detail in Section 4, where we also point out that in general this hole does not affect significantly the performance of the correlator. To achieve scale and rotation invariance, the amplitude of $\mathrm{V}(\mathrm{x},\mathrm{y})$ is transformed to the polar coordinate function, $\mathrm{F}(\mathrm{r},\theta)$, using the FPGA. Then it is converted to the log-polar coordinate function $\mathrm{G}(\rho,\theta)$ using the same FPGA. The reference images are polar Mellin transformed and stored in the database. The database can be a computer or a holographic memory disk if fast retrieval of the reference image is required. The captured query image also goes through the same procedure of PMT and is supplied to the correlator's input port. In the next section, we describe the PMT process in detail, including illustrative examples.

3. PREPROCESSING THE IMAGE USING POLAR MELLIN TRANSFORM AND EXAMPLES OF CORRELATIONS USING IDEALIZED IMAGES

A simple example of the PMT process is illustrated in Fig. 6. Here, we assume an artificial case, where the amplitude of the FT [i.e., $\mathrm{V}(\mathrm{x},\mathrm{y})$] of an image is chosen to be an uniform square, with a flower shape hole in it, as shown in Fig. 6(a). The corresponding polar function, $\mathrm{F}(\mathrm{r},\theta)$ is shown in Fig. 6(b) and the corresponding polar-logarithmic function, $\mathrm{G}(\rho,\theta)$ is shown in Fig. 6(c). Note that for $\mathrm{F}(\mathrm{r},\theta)$ the coordinates r and θ are rectilinear (as opposed to curvilinear). For a given combination of coordinates in polar space, say $\{\mathrm{r} = \mathrm{r}_1; \theta = \theta_1\}$, we determine the corresponding values of x and y by using the relations $\mathrm{x}_1 = \mathrm{r}_1 \cos\theta_1$ and $\mathrm{y}_1 = \mathrm{r}_1 \sin\theta_1$. The value of the function F is then given by $\mathrm{F}(\mathrm{r}_1,\theta_1) = |\mathrm{V}(\mathrm{x}_1,\mathrm{y}_1)|$. To plot the function F, we put the corresponding value of F at the coordinate $(\mathrm{x}_1,\mathrm{y}_1)$ to a point that is a distance r_1 away from the origin along the horizontal axis (which has the dimension of inverse length, mm^{-1}) and a distance θ_1 away from the origin along the vertical axis (which is in the dimension of radian and spans from 0 to 2π).

To generate the log-polar coordinate function $\mathrm{G}(\rho,\theta)$, we proceed as follows: for a given combination of coordinates in this space, say $\{\rho = \rho_1; \theta = \theta_1\}$, we determine the corresponding values of r and θ (i.e., r_1 and θ_1) by using the relations $\rho_1 = \log(\mathrm{r}_1/\mathrm{r}_0)$ and $\theta_1 = \theta_1$. Here, the choice of the scaling distance, r_0, is arbitrary. Note that the value of $\log(\mathrm{r}_1/\mathrm{r}_0)$ approaches $-\infty$ as r approaches zero, for any finite value of r_0. Obviously, this is an impractical situation. To circumvent this problem, we choose to ignore the information contained in a small circle of radius r_0 (in the $\mathrm{V}(\mathrm{x},\mathrm{y})$ plane), centered around $\mathrm{r} = 0$, thus restricting the lower range of $\rho = \log(\mathrm{r}/\mathrm{r}_0)$ to 0, corresponding to $\mathrm{r} = \mathrm{r}_0$. The magnitude of r_0 should be chosen judiciously so as not to exclude any critical feature that may be present within the exclusion zone of $0 \le \mathrm{r} \le \mathrm{r}_0$. Of course, for the particular case shown in Fig. 6, already a dark part in the center of $\mathrm{V}_\mathrm{A}(\mathrm{x},\mathrm{y})$. Thus there is no loss of information if the circle of radius r_0 is fully contained in the small dark part. Figures 7(b) and 7(c) show the amplitude and the phase, respectively, of the image whose magnitude of FT is $\mathrm{V}_\mathrm{A}(\mathrm{x},\mathrm{y})$ as shown in Fig. 7(a). From Fig. 7(c), it is clear that such an image whose magnitude of the FT is $\mathrm{V}_\mathrm{A}(\mathrm{x},\mathrm{y})$ is unrealistic because the phase of the actual image is spanning between $-\pi$ to π. While in this section we restrict ourselves to unrealistic images, where FTs have holes at the center, in Section 4 we will consider realistic images, for which it would be essential to exclude a small circle in FT plane.

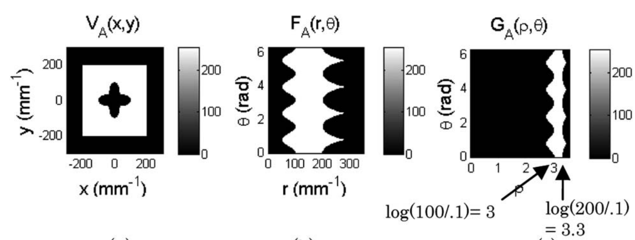

(a) (b) (c)

Fig. 6. (a) $\mathrm{V}(\mathrm{x},\mathrm{y})$ is the amplitude of the FT of an image with a flower shape hole in it. (b) Corresponding polar function, $\mathrm{F}(\mathrm{r},\theta)$ is shown. (c) Polar-logarithmic function, $\mathrm{G}(\rho,\theta)$ is shown [here, $\mathrm{r}_0 = 0.1$].

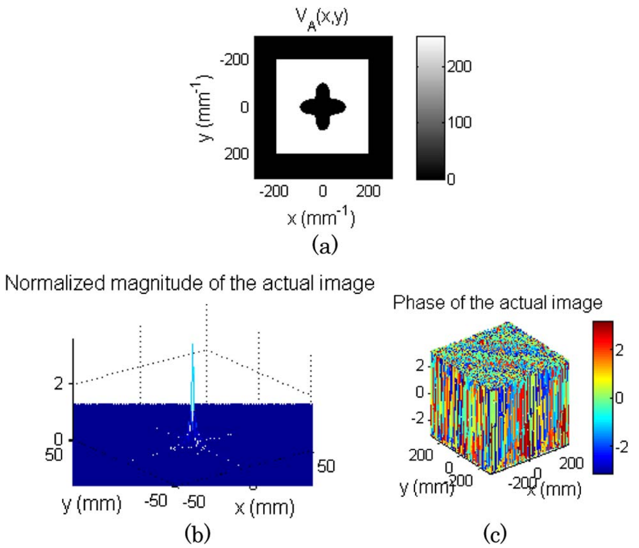

Fig. 7. (a) Shows $V_A(x, y)$, which is the FT of an image. (b) Shows the magnitude of an image whose FT is $V_A(x, y)$. (c) Shows the phase of the actual image whose FT is $V_A(x, y)$.

Before proceeding further, we note that the necessity of excluding a small circle in the FT plane was not addressed in the previous original investigations [11,12] pertaining to the use of PMTs for rotation and scale invariant correlations. This is due in part to the fact that these papers considered artificial images, where FTs already contained holes in the center. Any realistic image, on the other hand, is bound to have a nonzero value at the center of the FT, corresponding to the average value of the image amplitude. However, in later work involving this approach, this issue was addressed [16,17].

Consider now a situation where two identical PMT images, each corresponding to Fig. 6(c), are applied as inputs to the HOC. The resulting final output signal, $|S_f|^2$ of the HOC, is illustrated in Fig. 8(a). Because of the perfect match, the output has a sharp peak at the center, corresponding to the sum of the terms T_3 and T_4 (which are identical in this case) of Eq. (10). The value (~1) at the peak, of course, is arbitrary, depending on the magnitude of the images. In Fig. 8(b), we show the peak clearly by applying a threshold value of 0.9.

Next we consider the effect of scale change on this PMT conversion process. Figure 9 shows such a case, where $V_A(x, y)$ represents the amplitude of the FT of the same image as considered in Fig. 6, and $V_B(x, y)$ represents the amplitude of the FT of the same image, but scaled *up* by a linear factor of $\sigma = 2$ (i.e., $\times 4$ larger in area). Thus $V_B(x, y)$ is scaled *down* by a linear factor of 2 ($\times 4$ smaller in area) compared with $V_A(x, y)$. Note first that the corresponding polar distributions [as shown in Figs. 9(b) and 9(e)], $F_B(r, \theta)$ and $F_A(r, \theta)$ are the same in the θ direction, but differ by the linear scaling factor (2 in this case) in the r direction. Note next that the corresponding polar-logarithmic distributions, $G_A(\rho, \theta)$ and $G_B(\rho, \theta)$ as shown in Fig. 9(c) and 9(f), respectively, are identical in shape, except for a shift in the ρ direction, equaling the logarithm of the scale factor: $\log(2) \cong 0.3$. This illustrates the essence of how scale invariance is achieved via these transformations. The FTs of $G_A(\rho, \theta)$ and $G_B(\rho, \theta)$ would be identical in amplitudes, thus leading to a strong cross-correlation when applied to the HOC, which eliminates the effect of relative shift.

Figures 9(g) and 9(h) illustrate the output signals of the HOC, if these PMT images [(G_A and G_B)] are applied as

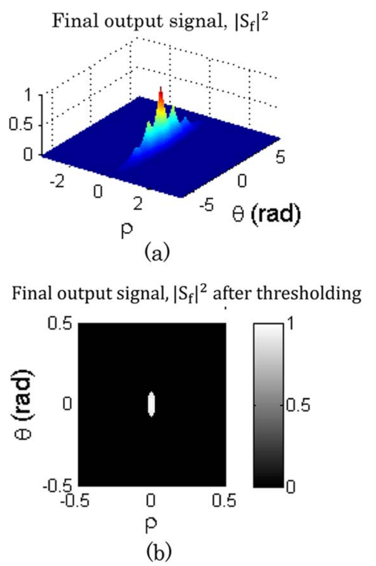

Fig. 8. (a) Final output signal when two identical images are inputs to the HOC. The PMT version is shown in Fig. 6(c). (b) Output signal after thresholding shows that there is a peak in the center when match between two objects is found.

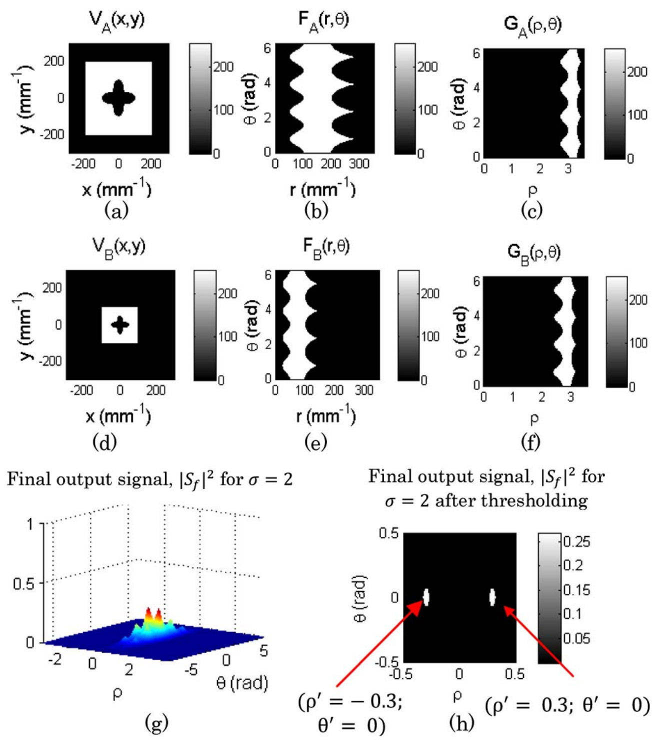

Fig. 9. (a) We consider an artificial case, where $V_A(x, y)$ is the FT of an image. (b) Corresponding polar distribution $F_A(r, \theta)$. (c) Corresponding log-polar distribution $G_A(\rho, \theta)$ (d) $V_B(x, y)$ is smaller in area than $V_A(x, y)$ by a factor of 4. (e) Corresponding polar distributions, $F_B(r, \theta)$. $F_B(r, \theta)$ and $F_A(r, \theta)$, are the same in the θ direction, but differ by the linear scaling factor (2 in this case) in the r direction. (f) Corresponding polar-logarithmic distribution, $G_B(\rho, \theta)$. $G_A(\rho, \theta)$ and $G_B(\rho, \theta)$ are identical in shape, except for a shift in the ρ direction [equaling the logarithm of the scale factor: $\log(2) \cong 0.3$]. (g) Final output signal $|S_f|^2$ when $G_A(\rho, \theta)$ and $G_B(\rho, \theta)$ are applied to the correlator. (h) Final signal after thresholding for $\sigma = 2$.

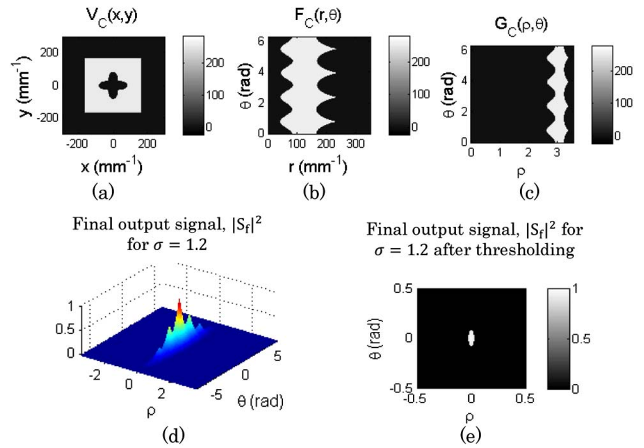

Fig. 10. (a) $V_C(x, y)$ is smaller in area than $V_A(x, y)$ by a factor of 1.44. (b) Corresponding polar distributions, $F_C(r, \theta)$. (c) Corresponding polar-logarithmic distribution is $G_C(\rho, \theta)$. (d) Final output signals $G_A(\rho, \theta)$ and $G_C(\rho, \theta)$ are applied to HOC. Final output signal has one peak at the center implying that a match is found, but no scale information is revealed due to the fact that the displacement between $G_A(\rho, \theta)$ and $G_C(\rho, \theta)$ is very small. (d) Final signal after thresholding for $\sigma = 1.2$.

inputs. The output signal of the correlator, $|S_f|^2$ contains the two cross-correlation terms, T_3 and T_4. From Eq. (10), T_3 represents the cross-correlation of the PMT images, $G_A(\rho, \theta) \odot G_B(\rho, \theta)$ and T_4 represents the anticross-correlation of the same PMT images, but in reverse order: $G_B(\rho, \theta) \odot G_A(\rho, \theta)$. Thus T_3 and T_4 signals are shifted by an equal amount but in the opposite direction according to the shift in position between $G_A(\rho, \theta)$ and $G_B(\rho, \theta)$. As shown in Fig. 9(g), the output now contains two peaks: (a) the cross-correlation, $G_A(\rho, \theta) \odot G_B(\rho, \theta)$ at $\rho' = \log(2) = 0.3$ and $\theta' = 0$ and (b) the anti-cross-correlation $G_B(\rho, \theta) \odot G_A(\rho, \theta)$ at $\rho' = -\log(2) = -0.3$ and $\theta' = 0$, where (ρ', θ') are the coordinates in the correlation plane. Here, as expected, the magnitude of each peak is ~0.27, which is approximately one fourth of the peak value shown in Fig. 8. In Fig. 9(h), we apply a threshold of 0.25 to illustrate the peaks clearly.

It is important to consider the limit imposed on this process by the fact that the final signal contains both T_3 and T_4 terms.

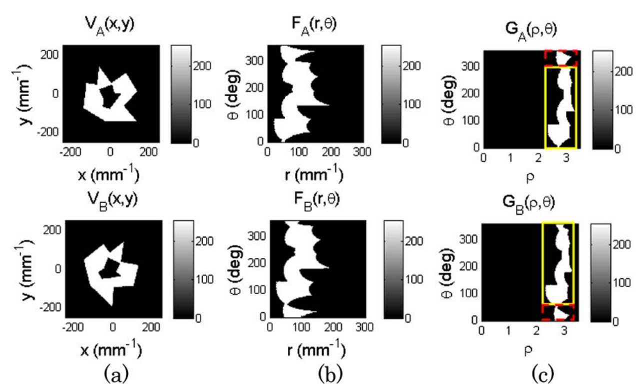

Fig. 11. (a) $V_A(x, y)$ is the amplitude of the FT of an arbitrary image and $V_B(x, y)$ represents the amplitude of the FT of the same image, but rotated by an angle of $\theta_0 = 45°$. (b) Corresponding polar distributions, $F_B(r, \theta)$ and $F_A(r, \theta)$, now differ in the θ direction. (c) Dotted part of $G_B(\rho, \theta)$ is now shifted from the solid part of $G_A(\rho, \theta)$ in the θ direction by an amount of $\theta_0 = 45°$; the dotted part of $G_B(\rho, \theta)$ is now shifted from the solid part of $G_A(\rho, \theta)$ in the θ-direction by an amount of $-(2\pi - \theta_0) = -315°$.

As we discussed in detail in Section 2, there are essentially two distinct scenarios, characterized by the parameter η. For the scale invariant recognition, the value of this parameter is proportional to the scaling factor. The case shown in Fig. 9 corresponds to $\eta > 1$, producing two peaks that are clearly resolved. We next consider a case where the scaling factor is small, corresponding to $\eta < 1$. In this case, $V_C(x, y)$ is scaled *down* by a small factor of $\sigma = 1.2$ compared with $V_A(x, y)$ as shown in Fig. 10(a). The corresponding polar distribution and log-polar distributions, $F_C(r, \theta)$ and $G_C(\rho, \theta)$, are shown in Figs. 10(b) and 10(c), respectively. For this case, the polar-logarithmic distributions, $G_A(\rho, \theta)$ and $G_C(\rho, \theta)$, are shifted from one another by an amount $\log(1.2) \approx 0.08$, which corresponds to $\eta < 1$.

Figure 10(d) shows the final signal while $G_A(\rho, \theta)$ and $G_C(\rho, \theta)$ are applied as input to the HOC architecture. In this case, the corresponding shift between $G_A(\rho, \theta)$ and $G_C(\rho, \theta)$ is $\log(1.2) \approx 0.08$. Hence, the two peaks have merged into a single peak of magnitude ~0.7. Note that in this case, while we are still able to determine the fact that the images are matched, the information about the relative scale between the images is lost. Figure 10(e) shows the final output signal after thresholding.

Now we consider the effect of rotation on the PMT images. Figure 11 shows such a case, where $V_A(x, y)$ is the amplitude of the FT of another arbitrary image, and $V_B(x, y)$ represents the amplitude of the FT of the same image, but rotated by an angle of $\theta_0 = 45°$. Thus $V_B(x, y)$ is rotated by an angle of $\theta_0 = 45°$ compared to $V_A(x, y)$. Here, we have made use of the well-known fact that the process of FT preserves the angular information. Note first that the corresponding polar distributions [as shown in Fig. 11(b)], $F_B(r, \theta)$, and $F_A(r, \theta)$ now differ in the θ direction only, and the pattern is shifted by $\theta_0 = 45°$. Also note that the log-polar distributions are now still identical in shapes, except that $G_B(\rho, \theta)$ is now shifted from $G_A(\rho, \theta)$ in the θ direction. It is particularly important to carefully consider the shift in the θ direction, since this coordinate is limited to a range of θ to 2π (360°). Specifically, the distribution along the θ direction in $G_A(G_B)$ can be broken into two parts: the part enclosed in the solid box in the upper (lower) part of Fig. 11(c) can be denoted as $G_{A1}(G_{B1})$, and the part enclosed in the dotted box is denoted as $G_{A2}(G_{B2})$. In $G_B(\rho, \theta)$, the G_{B1} part is shifted by an angle θ_0, while the GB_2 part is shifted by $-(2\pi - \theta_0)$, compared to G_{A1} & G_{A2}, respectively. Figure 12(a) shows the cross-correlation (T_3) and anti-cross-correlation signal (T_4), when $G_A(\rho, \theta)$ and $G_B(\rho, \theta)$ are applied to the HOC. Figure 12(b) shows the cross-sectional view (as a function of θ for $\rho = 0$) of the cross-correlation (T_3) and anti-cross-correlation signal (T_4). Consider first the T_3 term, which corresponds to $G_A(\rho, \theta) \odot G_B(\rho, \theta)$. Since there is no match between $G_{A1}(\rho, \theta)$ and $G_{B2}(\rho, \theta)$ and between $G_{A2}(\rho, \theta)$ and $G_{B1}(\rho, \theta)$, we get only two peaks: peak 3a corresponding to $G_{A1}(\rho, \theta) \odot G_{B1}(\rho, \theta)$ at $\rho' = 0$ and $\theta' = \theta_0$ (= 45°), and peak 3b corresponding to $G_{A2}(\rho, \theta) \odot G_{B2}(\rho, \theta)$ at $\rho' = 0$ and $\theta' = -(2\pi - \theta_0) = -315°$. The signal corresponding to T_3, for $\rho = 0$, is plotted as a function of θ in Fig. 12(c). As can be seen, peak 3a is prominent, while peak 3b is barely visible. This is due to the fact that θ_0 is small compared to $(2\pi - \theta_0)$ so that the energy contained in $G_{A2}(G_{B2})$ is smaller than that contained in $G_{A1}(G_{B1})$. Similarly, from the T_4 term, we get two other peaks: peak 4a corresponding to

$G_{B1}(\rho,\theta) \odot G_{A1}(\rho,\theta)$ at $\rho' = 0$ and $\theta' = -\theta_0$; and peak 4b corresponding to $G_{B2}(\rho,\theta) \odot G_{A2}(\rho,\theta)$ at $\rho' = 0$ and $\theta' = (2\pi - \theta_0)$. These two peaks are shown in Fig. 12(d), as a function of θ, for $\rho' = 0$. Again, we see that peak 4b is much smaller than peak 4a. The final output signal $|S_f|^2$ is shown in Fig. 12(e). Here, we see peaks 3a and 4a clearly, while peaks 3b and 4b are barely visible. However, the detection of just two peaks is enough to discern the relative angle of rotation. Figure 12(f) shows the final output signal $|S_f|^2$ after thresholding from where the locations of the peaks are clearly visible. In Fig. 13, we show how the relative amplitudes of peaks 3a and 3b vary as a function of the rotation angle, θ_0. Similar behavior occurs (not shown) for peaks 4a and peak 4b as well. The actual ratios of these peaks would, of course, depend on the details of the angular properties of the image.

Next we consider the effect of rotation and scale change simultaneously. Figure 14 shows such a case, where $V_A(x,y)$ is the amplitude of the FT of an arbitrary image and $V_C(x,y)$ represents the amplitude of the FT of the same image, but scaled *up* by a linear factor of 2 and rotated by an angle of $\theta_0 = 45°$. Note first that the corresponding polar distributions [as shown in Fig. 14(b)], $F_C(r,\theta)$, and $F_A(r,\theta)$ now differ in

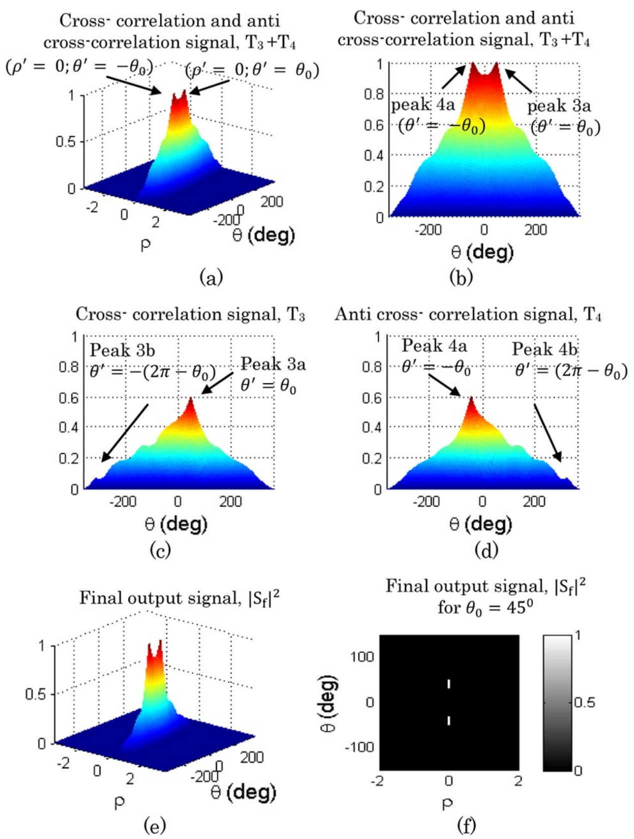

Fig. 12. (a) Cross-correlation and anti-cross-correlation $(T_3 + T_4)$ signal when $G_A(\rho,\theta)$ and $G_B(\rho,\theta)$ are applied to the HOC. (b) Cross-sectional view of the $T_3 + T_4$ signal showing two peaks shifted in the θ direction by an amount of θ_0 and $-\theta_0$, which correspond to the cross-correlation terms $G_{A1}(\rho,\theta) \odot G_{B1}(\rho,\theta)$ and $G_{B1}(\rho,\theta) \odot G_{A1}(\rho,\theta)$. (c) Cross-correlation signal T_3, which shows the two peaks corresponding to the cross-correlation $G_{A1}(\rho,\theta) \odot G_{B1}(\rho,\theta)$ and $G_{A2}(\rho,\theta) \odot G_{B2}(\rho,\theta)$. (d) Anti-cross-correlation signal T_4, which shows the two peaks corresponding to the cross-correlations $G_{B1}(\rho,\theta) \odot G_{A1}(\rho,\theta)$ and $G_{B2}(\rho,\theta) \odot G_{A2}(\rho,\theta)$. (e) Final output signal $|Sf|^2$. (f) Final output signal after thresholding.

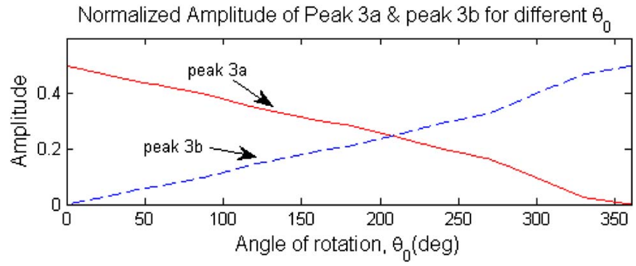

Fig. 13. Normalized amplitude of T_3 for different angles. See text for details.

both the r direction and the θ direction. Note next that the log-polar distributions are now still identical in shapes, except that $G_C(\rho,\theta)$ is now shifted from $G_A(\rho,\theta)$ in the ρ direction by an amount, $\rho_0 = \log(2) = 0.3$, and the θ direction by an amount, $\theta_0 = 45°$. Similar to the case of rotation change described above, the distribution along the θ direction in $G_A(G_C)$ can be broken into two parts: the part enclosed in the solid box in the upper (lower) part of Fig. 14(c) can be denoted as $G_{A1}(G_{C1})$, and the part enclosed in the dotted box is denoted as $G_{A2}(G_{C2})$. In $G_C(\rho,\theta)$ the G_{C1} part is shifted by an angle θ_0, while the G_{C2} part is shifted by $-(2\pi - \theta_0)$, compared with G_{A1} and G_{A2}, respectively.

Figure 15(a) shows the cross-correlation and anti-cross-correlation $(T_3 + T_4)$ signal, when $G_A(\rho,\theta)$ and $G_C(\rho,\theta)$ are applied to the HOC. The output contains several peaks, corresponding to the cross-correlation and anti-cross-correlation terms, T_3 and T_4, of Eq. (9). Consider first the T_3 term, which corresponds to $G_A(\rho,\theta) \odot G_C(\rho,\theta)$. Since, there is no match between $G_{A1}(\rho,\theta)$ and $G_{C2}(\rho,\theta)$ and between $G_{A2}(\rho,\theta)$ and $G_{C1}(\rho,\theta)$, we get only two strong peaks: peak 3a′ corresponding to $G_{A1} \odot G_{C1}(\rho,\theta)$ at $\rho' = \log(2) = 0.3$ and $\theta' = \theta_0$ $(= 45°)$, and peak 3b′ corresponding to $G_{A2}(\rho,\theta) \odot G_{C2}(\rho,\theta)$ at $\rho' = 0.3$ and $\theta' = -(2\pi - \theta_0)$ [shown in Fig. 15(c)]. As can be seen, peak 3a′ is prominent, while peak 3b′ is barely visible. Similarly, from the T_4 term, we get two other peaks: peak 4a′ corresponds to $G_{C1}(\rho,\theta) \odot G_{A1}(\rho,\theta)$ at $\rho' = -0.3$ and $\theta' = -\theta_0$; and peak 4b′ corresponds to $G_{C2}(\rho,\theta) \odot G_{A2}(\rho,\theta)$ at $\rho' = -0.3$ and $\theta' = (2\pi - \theta_0)$ [shown in Fig. 15(d)]. Figure 15(e) shows the final output signal $|S_f|^2$, and Fig. 15(f) shows the output signal after applying a threshold of 0.9. From Fig. 15(f), it is obvious that the

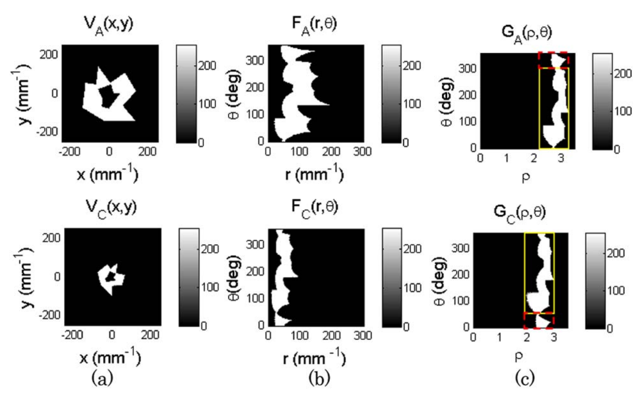

Fig. 14. (a) $V_C(x,y)$ is smaller in area by a factor of 4 than $V_A(x,y)$ and is rotated by 45°. (b) Corresponding polar distributions, $F_C(r,\theta)$ and $F_A(r,\theta)$, now differ in the r direction and the θ direction. (c) $G_C(\rho,\theta)$ is now shifted from $G_A(\rho,\theta)$ in the ρ direction by an amount $\log(2) = 0.3$ and the θ direction by an amount of $\theta_0 = 45°$.

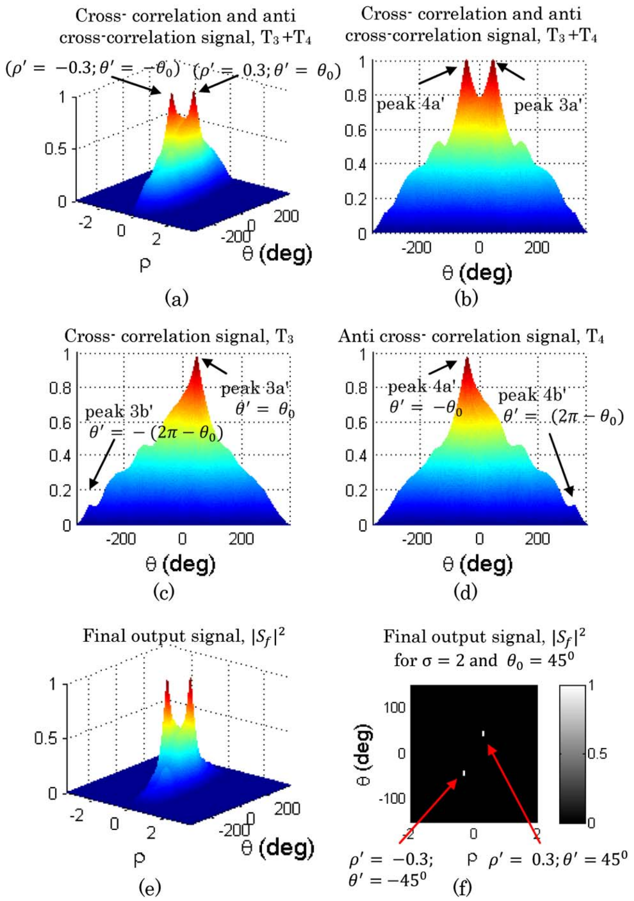

Fig. 15. (a) Cross-correlation and anti-cross-correlation ($T_3 + T_4$) signal when $G_A(\rho, \theta)$ and $G_C(\rho, \theta)$ are applied to the HOC, showing two peaks at ($\rho' = 0.3; \theta' = 45°$) and ($\rho' = -0.3; \theta' = -45°$). These correspond to the cross-correlation terms $G_{A1}(\rho, \theta) \odot G_{C1}(\rho, \theta)$ and $G_{C1}(\rho, \theta) \odot G_{A1}(\rho, \theta)$, respectively. (b) Cross-sectional view shows the peaks 3a′ and 4a′. (c) Cross-correlation signal T_3, which shows the two peaks corresponding to the cross-correlation $G_{A1}(\rho, \theta) \odot G_{C1}(\rho, \theta)$ and $G_{A2}(\rho, \theta) \odot G_{C2}(\rho, \theta)$. (d) Anti-cross-correlation signal T_4, which shows the two peaks corresponding to the cross-correlations $G_{C1}(\rho, \theta) \odot G_{A1}(\rho, \theta)$ and $G_{C2}(\rho, \theta) \odot G_{A2}(\rho, \theta)$ (e) Final output signal $|Sf|^2$. (f) Final output signal after thresholding.

positions of the peak of the cross-correlation signal (T_3) corresponds to rotation and scale change between two images.

4. SIMULATION RESULTS OF THE SCALE AND ROTATION INVARIANT HOC

In Section 3, we have shown that by incorporating PMT, the proposed HOC architecture can achieve scale and rotation invariance, in addition to the shift invariance feature. So far, we have considered artificial cases, where the FT of the object or reference image has a distinct hole in the center. As discussed earlier, this corresponds to an unrealistic situation, where the image must have both positive and negative amplitudes. In this section, we consider real world scenarios, where the image has non-negative values everywhere. Since such an image has a nonzero average value, its FT cannot have a hole in the center. By cutting a hole of a suitable radius in the center of the FT of the image, we produce an effective image, which is no longer positive definite and is thus compatible with the PMT process.

In Fig. 16(a), we consider two images, $U_1(x', y')$ and $U_2(x', y')$, where $U_2(x', y')$ is scaled down by a linear factor of 2 with respect to $U_1(x', y')$. The corresponding magnitudes of FTs, $V_1(x, y)$ and $V_2(x, y)$, are shown in Fig. 16(b), where $V_2(x, y)$ is scaled up by a factor of 2 compared to $V_1(x, y)$ in each dimension. Here, we take the magnitude of the FTs to get rid of any shift information. In Fig. 16(c), a hole of radius r_0 is created in the center of $V_1(x, y)$ and $V_2(x, y)$, which are denoted as $V_{1H}(x, y)$ and $V_{2H}(x, y)$, respectively. Figure 16(d) shows the corresponding polar distributions, $F_1(r, \theta)$ and $F_2(r, \theta)$. As shown in Fig. 16(e), the polar-logarithmic distributions are nearly identical in shape, except that $G_2(\rho, \theta)$ is now shifted from $G_1(\rho, \theta)$ in the ρ direction by an amount of $\log(2) = 0.3$. The PMT processed images, $G_1(\rho, \theta)$ and $G_2(\rho, \theta)$, are now inputs to the HOC architecture. Figure 16(f) shows the final output signals $|S_f|^2$ of the HOC, where the peaks of the cross-correlation signals, T_3 and T_4, are shifted from the center in the ρ direction by an amount equaling $\log(\sigma)$ and $-\log(\sigma)$, respectively. Figure 16(g) shows that thresholding gives a clear view of the location of these peaks, from which we can determine the relative scaling factor. When a hole is cut in the FT of an image, the process is equivalent to the use of a modified image. We use one of the images considered above, $U_1(x', y')$, to illustrate what this modified image looks like. Before proceeding, it is instructive to document clearly the notations we have employed (as shown in Table 1).

In the correlation process described in Fig. 16, we made use of $V_{1H}(x, y)$ and $V_{2H}(x, y)$. The corresponding modified images are $U_{1H}(x', y')$ and $U_{2H}(x', y')$. As an example, we show below, in steps, how to determine $U_{1H}(x', y')$ and explain its shape. Figure 17(a) shows $V_1(x, y)$, the FT of the original image, while Fig. 17(e) shows $V_{1H}(x, y)$, the FT of the modified image. However, in order to reconstruct the corresponding images, we require the complex FTs. These are illustrated next. Figures 17(b) and 17(c) show the real and imaginary parts respectively of $\tilde{U}_1(k_{x'}, k_{y'}) = \tilde{U}_1(x, y)$, the FT of the original image. Inverse FT of $\tilde{U}_1(x, y)$ yields the original image, $U_1(x', y')$, which is shown in axonometric view in Fig. 17(d). Note that the original image is real only. Similarly, Figs. 17(f) and 17(g) show the real and imaginary parts, respectively, of $\tilde{U}_{1H}(k_{x'}, k_{y'}) = \tilde{U}_{1H}(x, y)$, the FT of the modified image. Inverse FT of $\tilde{U}_{1H}(x, y)$, yields the modified image, $U_{1H}(x', y')$. Note that $U_{1H}(x', y')$ is complex, as a result of the hole-cutting process. Real and imaginary parts of $U_{1H}(x', y')$ are shown in Figs. 17(h) and 17(i), respectively.

In Fig. 18(a), we consider two images, $U_1(x', y')$ and $U_3(x', y')$, where $U_3(x', y')$ is scaled down by a linear factor of 2 and also rotated with respect to $U_1(x', y')$ by an angle of $\theta_0 = 30°$. The magnitude of the FT of $U_3(x', y')$, denoted as $V_3(x, y)$, is also rotated by an angle of $\theta_0 = 30^0$, and the area is enlarged by a factor of 4, as shown in Fig. 18(b). In Fig. 18(c), a hole of radius r_0 is created in the center of each of $V_1(x, y)$ and $V_3(x, y)$, producing functions denoted as $V_{1H}(x, y)$ and $V_{3H}(x, y)$, respectively. The corresponding polar distributions, $F_1(r, \theta)$ and $F_3(r, \theta)$, are shown in Fig. 18(d). As shown in Fig. 18(e), the polar-logarithmic distributions are still identical in shape, except that $G_3(\rho, \theta)$ is shifted from $G_1(\rho, \theta)$ in the θ direction and ρ direction. In the process described above, two original images, $U_1(x', y')$ and $U_3(x', y')$, are converted to PMT images, $G_1(\rho, \theta)$, and $G_3(\rho, \theta)$, which

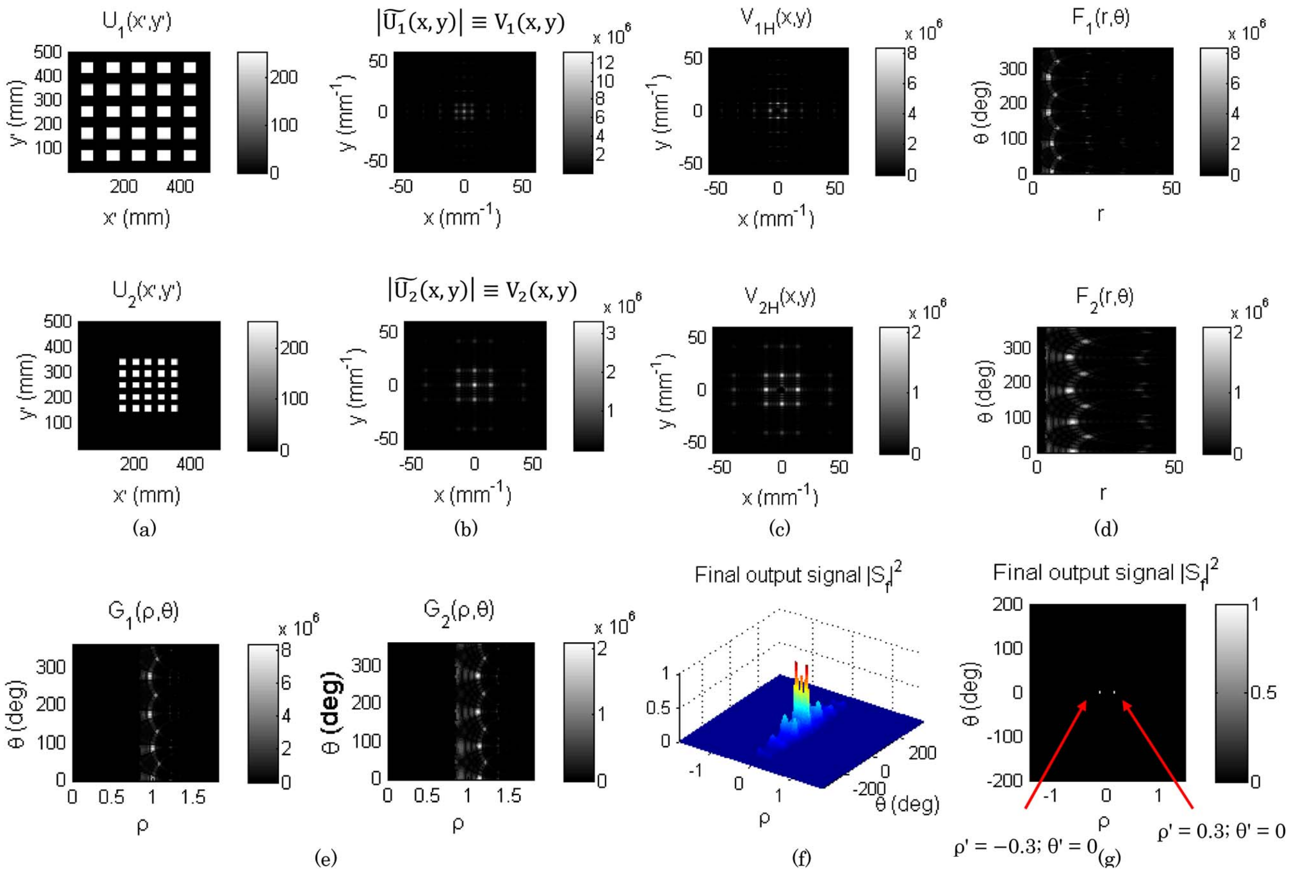

Fig. 16. (a) We consider two images, $U_1(x', y')$ and $U_2(x', y')$, where $U_2(x', y')$ is smaller in area than $U_1(x', y')$ by a factor of 4. (b) The corresponding magnitudes of FTs are denoted as $V_1(x, y)$ and $V_2(x, y)$, which are similar in shape, except that $V_2(x, y)$ has a larger area than that of $V_1(x, y)$ by a factor of 4. (c) A hole of radius r_0 is created in the center of $V_1(x, y)$ and $V_2(x, y)$, and the resulting functions are denoted as $V_{1H}(x, y)$ and $V_{2H}(x, y)$, respectively. (d) The corresponding polar distributions, $F_1(r, \theta)$ and $F_2(r, \theta)$, are the same in the θ direction, but differ by a linear scaling factor of 2 in the r direction. (e) The polar-logarithmic distributions, $G_1(\rho, \theta)$ and $G_2(\rho, \theta)$, are identical in shape, except for a shift in the ρ direction [equaling the logarithm of the scale factor: $\log(2) \cong 0.3$]. (f) The final output signal, $|S_f|^2$ of the HOC when $U_1(x', y')$ and $U_2(x', y')$, is converted to the log-polar domain and then acts as an input to the HOC. (g) After thresholding, we get two peaks corresponding to the two cross-correlation terms (T_3 and T_4).

Table 1. Summary of Definitions of Various Transform

Symbol	Meaning
$U_1(x', y')$	Original image; $\{x', y'\}$ are spatial coordinates, with units of millimeter (mm)
$\tilde{U}_1(k_{x'}, k_{y'})$	FT of the original image; $\{k_{x'}, k_{y'}\}$ are wave number coordinates, with units of mm^{-1}
$\tilde{U}_1(x, y)$	Same as $\tilde{U}_1(k_{x'}, k_{y'})$, except that we have defined $x \equiv k_{x'}$, $y \equiv k_{y'}$. Thus $\{x, y\}$ are wave number coordinates, with units of mm^{-1}. This redefinition is for convenience only.
$V_1(x, y) \equiv \lvert\tilde{U}_1(x, y)\rvert$	This is the magnitude of the FT of original image.
$U_{1H}(x', y')$	Image resulting from cutting a hole in the FT.
$\tilde{U}_{1H}(k_{x'}, k_{y'})$	FT of $U_{1H}(x', y')$; again $\{x', y'\}$ are spatial coordinates.
$\tilde{U}_{1H}(x, y)$	Same as $\tilde{U}_{1H}(k_{x'}, k_{y'})$ with the definition of $x \equiv k_{x'}$, $y \equiv k_{y'}$
$V_{1H}(x, y) \equiv \lvert\tilde{U}_{1H}(x, y)\rvert$	This is the magnitude of the FT of the modified image.

act as inputs to the HOC architecture. Fig. 18(f) shows the final results of the HOC architecture, where the cross-correlation signal T_3 has two peaks at positions ($\rho' = \log(\sigma)$, $\theta' = \theta_0$) and ($\rho' = \log(\sigma)$, $\theta' = -(2\pi - \theta_0)$) and the anti-cross-correlation signal, T_4 also has two peaks at positions ($\rho' = -\log(\sigma)$, $\theta' = -\theta_0$) and ($\rho' = -\log(\sigma)$, $\theta' = (2\pi - \theta_0)$). As mentioned in Section 3, the peaks at positions ($\rho' = \log(\sigma)$, $\theta' = -(2\pi - \theta_0)$) and ($\rho' = -\log(\sigma)$, $\theta' = (2\pi - \theta_0)$) are very small compared to other peaks, so that they are barely visible in the final output signal. Figure 18(g) shows that after thresholding the peaks of the cross-correlation signals at positions ($\rho' = \log(\sigma)$, $\theta' = \theta_0$) and ($\rho' = -\log(\sigma)$, $\theta' = -\theta_0$) are clearly visible. From the location of the peaks, we can infer that the objects are rotated with respect to each other by an angle of 30° and also scaled down by a factor of 2.

5. MULTIPLE OBJECT DETECTION USING THE HOC ARCHITECTURE

In [8], we showed how to recognize a single object using the HOC architecture in a shift invariant manner. In this paper so far, we have shown how to recognize a single object in a shift, scale, and rotation invariant manner. However, there are

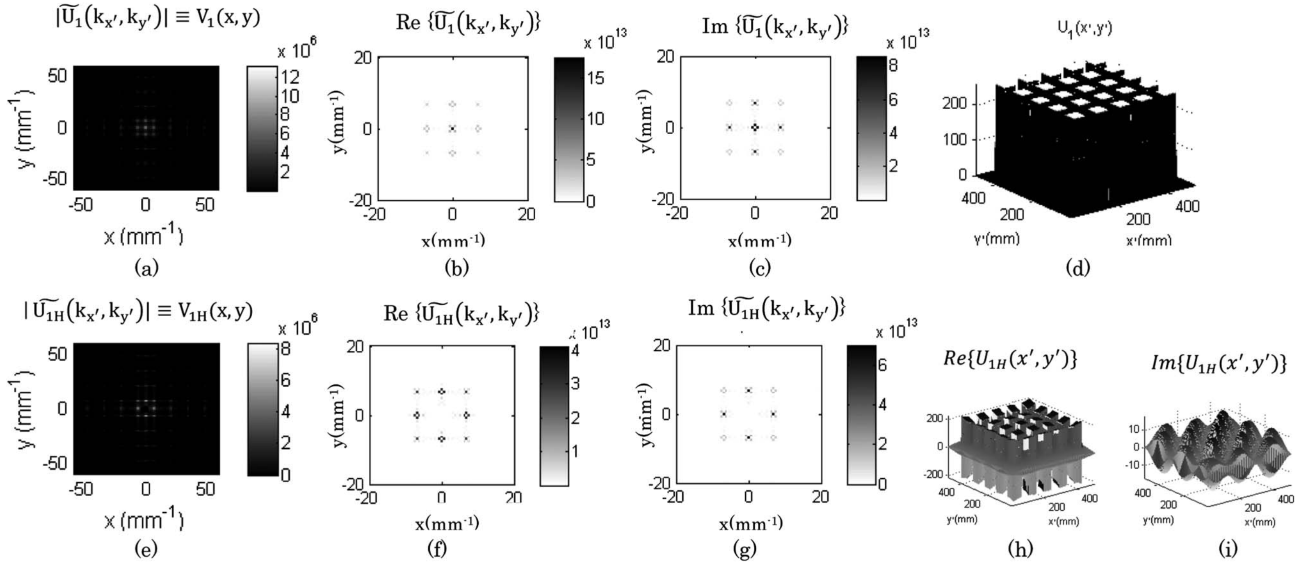

Fig. 17. Illustration of the fact that cutting a hole of certain radius in the center of the FT of the image does not change the image significantly. See text for details. [Note that in Figs. 18(b), 18(c), 18(f), and 18(g) the color has been inverted for clear visualization.]

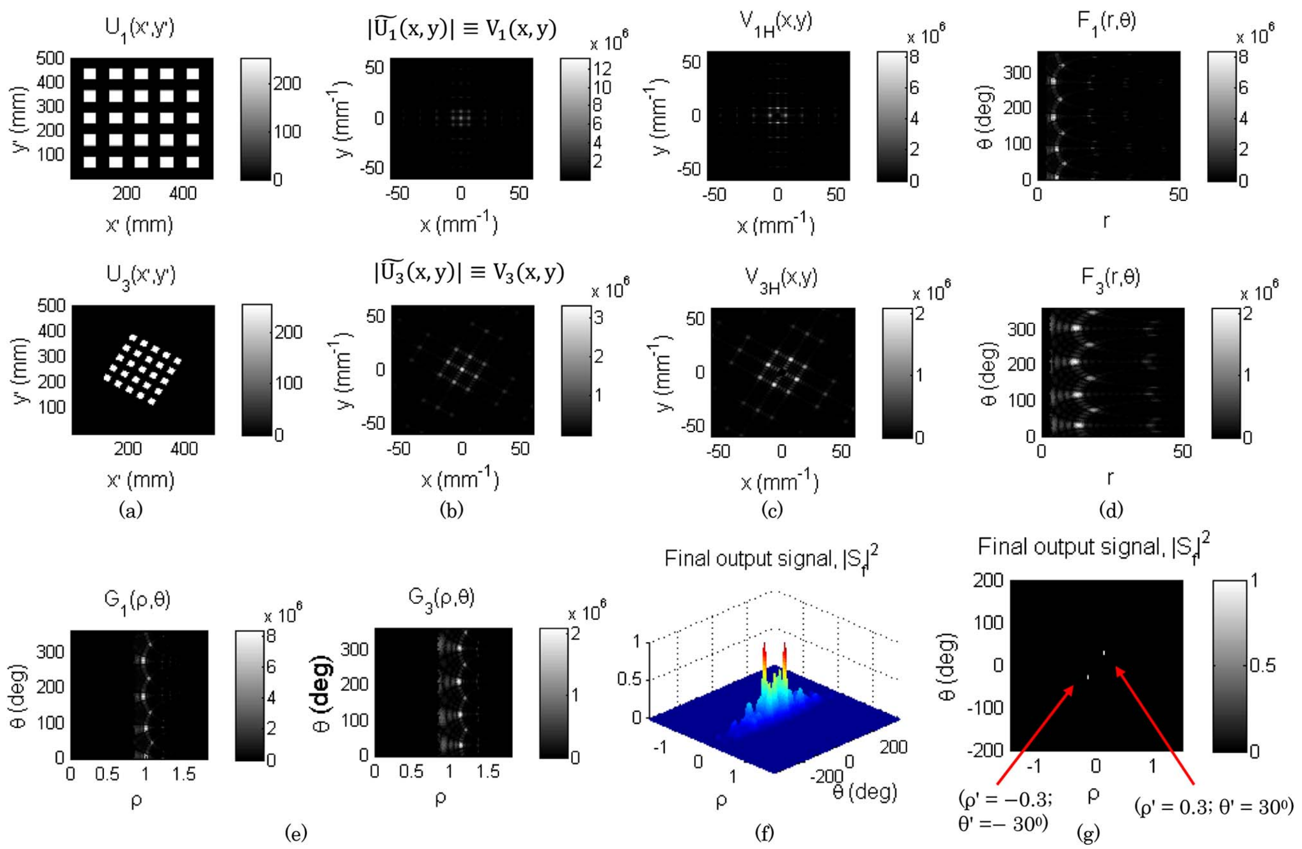

Fig. 18. (a) We consider two images, $U_1(x',y')$ and $U_3(x',y')$, where $U_3(x',y')$ is smaller in area than $U_1(x',y')$ by a factor of 4 and also rotated by an angle of $\theta_0 = 30°$. (b) The corresponding FTs are denoted as $V_1(x,y)$ and $V_3(x,y)$, which are similar in shape, except $V_3(x,y)$ has a larger area than that of $V_1(x,y)$ by a factor of 4 and also rotated by an angle of $\theta_0 = 30°$. (c) A hole of radius r_0 is created in the center of $V_1(x,y)$ and $V_3(x,y)$, which are denoted as $V_{1H}(x,y)$ and $V_{3H}(x,y)$, respectively. (d) The corresponding polar distributions, $F_1(r,\theta)$ and $F_3(r,\theta)$, are shifted in the θ direction by an amount of $\theta_0 = 30°$ and also shifted in the r direction by a linear scaling factor of 2. (e) Polar-logarithmic distributions, $G_1(\rho,\theta)$ and $G_3(\rho,\theta)$, are identical in shapes, except for a shift in the ρ direction [equaling the logarithm of the scale factor: $\log(2) \cong 0.3$] and also a shift in the θ-direction by an amount of $\theta_0 = 30°$. (e) Final output signal, $|S_f|^2$ of the HOC when $U_1(x',y')$ and $U_3(x',y')$ are converted to $G_1(\rho,\theta)$ and $G_3(\rho,\theta)$ and act as inputs to the HOC. (f) After thresholding, we get two peaks corresponding to the two cross-correlation terms (T_3 and T_4).

potential scenarios, where the query field may contain multiple matches to the reference object. In this section, we describe how to achieve distinct detection of these multiple matches. We consider two different scenarios.

First we consider the case, where the multiple images in the query field are only shifted, without any scale change and rotation angle. In this case, the architecture needed does not employ the PMT process. However, it is somewhat different from the approach used for detecting multiple (unscaled and unrotated) matches using a CHC because of the fact that the HOC produces both cross-correlation and anticross-correlation signals. Second we consider the case, where the multiple images in the query field have potentially distinct values of shift, scale factor, and rotation angle. In this case, the PMT process has to be employed. However, since the PMT process eliminates the shift information, multiple object recognition in this case requires a substantially different architecture.

A. Multiple Object Detection for Shifted Images without Rotation and Scale Change

Detection of multiple objects using the HOC architecture without rotation and scale change is similar to single object detection under the same scenario (i.e., without rotation and scale change), in that it does not require using the PMT process. However, a potential complication arises due to the presence of both T_3 (cross-correlation) and T_4 (anti-cross-correlation) terms. Specifically, in the presence of multiple matches, it becomes difficult to determine whether a peak corresponds to T_3 of a given matched image or T_4 of another matched image, for example. This can be circumvented by applying the following technique. Assume first that the reference image is represented by a grid of $N \times N$ points. In contrast, we confine the query image, potentially containing multiple objects, to a grid of only $N/2 \times N$ points. We now map this query image to a grid of $N \times N$ points, thus producing a final query image, where half the image is blank. Consider a situation, where the blank half of the query image is on the left side. It is easy to see that, after carrying out the correlation process in the manner described in Section 2, the peaks representing all the T_3's (corresponding to multiple matches) will appear on the right side of the final signal plane, while all the T_4's will appear on the left side of the final signal plane, thus avoiding the potential ambiguities between the T_3's and the T_4's mentioned above.

Figure 19 illustrates the results of a simulation for multiple-object detection with the HOC using this approach. Figure 19(a) shows the reference image, Im_A, plotted on an $N \times N$ grid. Figure 19(b) show the query image, Im_B, which contains three images that match the reference (denoted as B, C, and D), and one that does not (denoted as A). Note that these four images are confined to the right-half plane only, leaving the left-half blank. Figure 19(c) shows the output signal, $|S_f|^2$, where we can see six sharp peaks corresponding to cross-correlation signals (T_{3B}, T_{3C}, and T_{3D}) and anticross-correlation signals (T_{4B}, T_{4C}, and T_{4D}) of the three matched images. The other two signals in the output plane with lower peaks correspond to the cross-correlation (T_{3A}) and anti-cross-correlation (T_{4A}) signals for the unmatched case. After thresholding [as shown in Fig. 19(d)], the final signals are

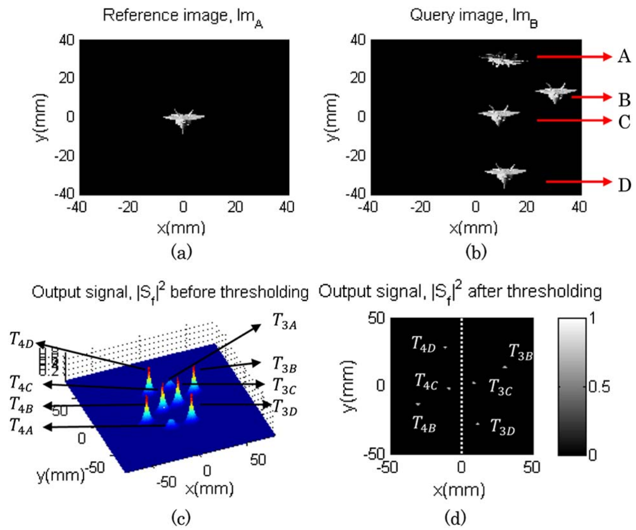

Fig. 19. Illustration of multiple object detection without rotation and scale change using the HOC architecture. See text for details.

clearly visible from which we can infer that three matches are found. In addition, the distances of the peaks from the center reveal the locations of the matched images.

This approach of leaving a blank space also has an added advantage, in that it ensures that the overlap parameter, η (defined in Section 2) is never less than unity. This can be seen clearly by considering image C, which is located at the left edge of the right-half plane. Since it is contained fully in the right-half plane, the distance between this and the reference images is $|\vec{\rho}_m|$, which corresponds to $\eta = 1$. All other images that are further away from the boundary between the left and right half planes would thus have a value of $\eta > 1$. Therefore, the cross-correlation and anti-cross-correlation signals will be clearly revolved for all images.

Finally, we note that the use of the rectangular field ($N/2 \times N$) in confining the query image may be inconvenient in some situations, especially if the camera used in acquiring the query image has an image field that is a square. This can be circumvented by confining the query image to a square field with $N/2 \times N/2$ points, leaving the other three quadrants blank.

B. Multiple Object Detection in Shift, Scale, and Rotation Invariant Manner Using the HOC Architecture

Next we consider a situation, where the query field contains multiple replicas of the reference image, but each with potentially a different position, a different scale factor, and a different angular orientation. Obviously, this case would require the use of the PMT process. However, the PMT process loses the information about the relative position of any image once the phase information in the FT is eliminated by measuring the magnitude of the FT. Thus the magnitude of the FTs of each of the matched images in the query field will overlap with one another, making it impossible to find any matches.

To overcome this problem, we propose the approach illustrated schematically in Figs. 20 and 21. The situation of interest here is as follows: we assume that we have one reference image, and $L \equiv n/2 \times n$ captured query images (n is an

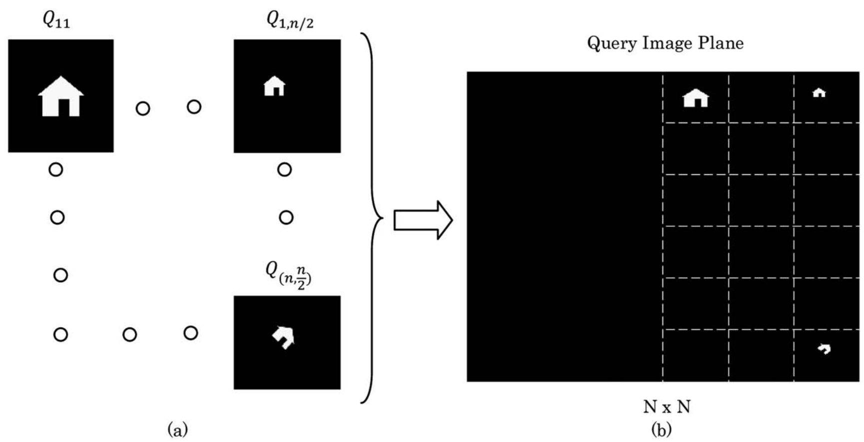

Fig. 20. Illustration of the process of mapping multiple query objects, each with potentially a different position, a different scale factor, and a different angular orientation, to the right half of the query image plane, which has a grid size of N × N. See text for details.

integer), each of which is a potentially shifted, scaled, and rotated replica of the reference image. In principle, we can employ the PMT-enhanced HOC process L times. The goal here is to carry out these L correlations simultaneously.

To start, we fit each captured image into a grid of (N/n) × (N/n), where N × N is the grid size for the reference image. We then fit these images into the right-half plane of an N × N grid. This is illustrated in Fig. 20. Next, we use an SLM to convert the query image to the optical domain. However, instead of sending the whole query image at once, we send to the SLM only one of the small grids (of size N/n × N/n) of the right-half plane with all the other small grids being dark. This is illustrated schematically shown on the left edge of the Fig. 21, for the first row and n/2-th column of the right-half plane, for example. The image in this grid is denoted as $Q_{1,n/2}$. The lens, the FPA, and the FPGA, as shown in the rest of Fig. 21, are used to produce the corresponding PMT image, denoted as $G_{1,n/2}(\rho,\theta)$. This process is repeated $n^2/2$ times, which is the number of small grids containing images, without changing the positions of the SLM, the lens, and the FPA. The $n^2/2$ numbers of PMT images produced and stored in the FPGA are then mapped to a corresponding set of small grids, which in turn is sent to the final SLM (SLM-3) for detecting cross-correlation and anti-cross-correlation signals.

In Fig. 22, we show results of numerical simulations used to illustrate the process described above. For simplicity, we have used an artificial reference image that has a clear hole in its FTs, similar to that shown earlier in Fig. 11. The FT of the reference image is shown in Fig. 22(a), denoted as F_{00}, and the FTs of multiple query objects are shown in Fig. 22(b), which are denoted as F_{ij} (i = row number; j = column number). For example, F_{42} is the image shown on the bottom right corner. The left half of the query plane is kept blank for the reason described above. As can be seen in Fig. 22(b), F_{21} and F_{42} are similar to F_{00}; F_{22} and F_{31} are rotated from F_{00} by an angle of $\theta_0 = 30°$; F_{11} and F_{32} are scaled down from F_{00} by a factor of $\sigma = 2$; F_{12} and F_{41} are scaled down by a factor of $\sigma = 2$ and also rotated by an angle of $\theta_0 = 30°$ from F_{00}. The corresponding PMT images, $G_1(\rho,\theta)$ and $G_2(\rho,\theta)$, are shown in Figs. 22(c) and 22(d), respectively [18]. Figure 22(e) shows the final signal $|S_f|^2$ after thresholding. The right-half side shows the cross-correlation signals and the left side shows the anti-cross-correlation signals. The red dots in Fig. 22(e) correspond to the auto-correlation of the reference PMT image, and the white dots on the right-half plane represent the corresponding cross-correlation signals. From the distance between the red dot and the white dot in a given box, we can infer the scale and rotation change between the reference image and the query image.

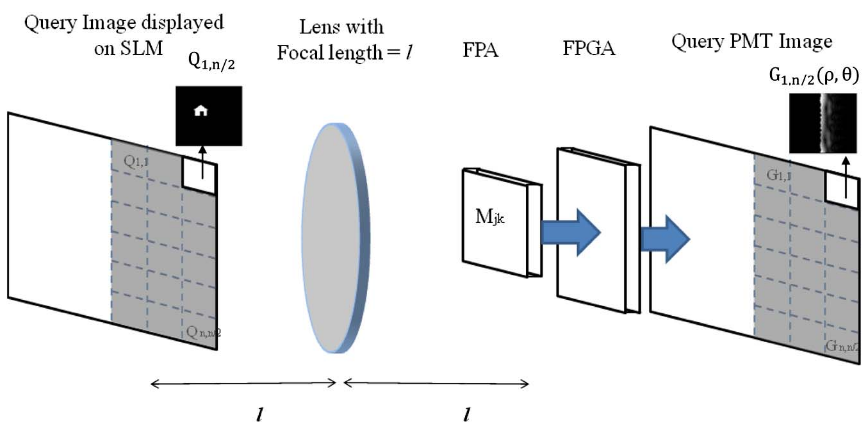

Fig. 21. Process of Fourier transforming a query image plane with multiple images using an SLM and a lens. See text for details.

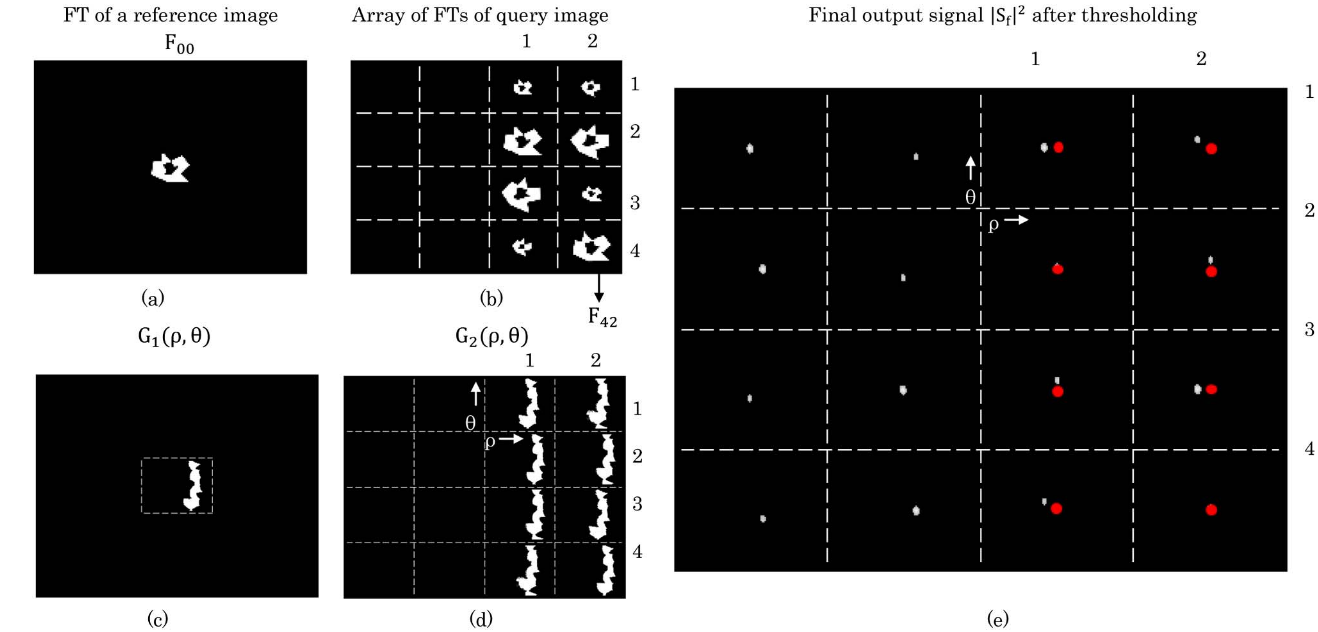

Fig. 22. (a) FT of the reference image. (b) Array of FTs of multiple objects, where one side is intentionally left blank. (c) PMT of the reference image. (d) PMT of the array of query images. (e) Final results from the HOC. We have to consider only the right half of this plane. See text for details.

6. CONCLUSIONS

We have shown that our proposed HOC architecture, which correlates images using SLMs, detectors, and FPGAs, is capable of detecting objects in a scale and rotation invariant manner, along with the shift invariance feature, by incorporating PMT. For realistic images, we cut out a small circle at the center of the Fourier transform (FT) domain, as required for PMT, and illustrate how this process corresponds to correlating images with real and imaginary parts. Furthermore, we showed how to carry out shift, rotation, and scale invariant detection of multiple matching objects simultaneously, a process previously thought to be incompatible with PMT based correlators. We presented results of numerical simulations to validate the concepts. Experimental efforts are underway in our laboratory to demonstrate these capabilities of the HOC using bulk components. Efforts are also underway to develop an integrated graphic processing unit [8] in order to realize a high-speed version of the HOC.

ACKNOWLEDGMENTS

This work is supported by AFOSR grant FA9550-10-01-0228, NSF CREST award 1242067, and NASA URC Group-V award NNX09AU90A.

REFERENCES AND NOTES

1. A. V. Lugt, "Signal detection by complex spatial filtering," IEEE Trans. Inf. Theory **10**, 139–145 (1964).
2. A. Heifetz, G. S. Pati, J. T. Shen, J.-K. Lee, M. S. Shahriar, C. Phan, and M. Yamomoto, "Shift-invariant real-time edge-enhanced Vander Lugt correlator using video-rate compatible photorefractive polymer," Appl. Opt. **45**, 6148–6153 (2006).
3. A. Heifetz, J. T. Shen, J.-K. Lee, R. Tripathi, and M. S. Shahriar, "Translation-invariant object recognition system using an optical correlator and a super-parallel holographic RAM," Opt. Eng. **45**, 025201 (2006).
4. J. Khoury, M. C. Golomb, P. Gianino, and C. Woods, "Photorefractive two-beam-coupling nonlinear joint-transform correlator," J. Opt. Soc. Am. B **11**, 2167–2174 (1994).
5. Q. Tang and B. Javidi, "Multiple-object detection with a chirp-encoded joint transform correlator," Appl. Opt. **32**, 5079–5088 (1993).
6. T. H. Barnes, K. Matsuda, T. Eiju, K. Matsumoto, and F. Johnson, "Joint transform correlator using a phase-only spatial light modulator," Jpn. J. Appl. Phys. **29**, L1293–L1296 (1990).
7. M. S. Shahriar, R. Tripathi, M. Kleinschmit, J. Donoghue, W. Weathers, M. Huq, and J. T. Shen, "Superparallel holographic correlator for ultrafast database searches," Opt. Lett. **28**, 525–527 (2003).
8. M. S. Monjur, S. Tseng, R. Tripathi, J. Donoghue, and M. S. Shahriar, "Hybrid optoelectronic correlator architecture for shift invariant target recognition," J. Opt. Soc. Am. A **31**, 41–47 (2014).
9. B. Javidi and C. Kuo, "Joint transform image correlation using a binary spatial light modulator at the Fourier plane," Appl. Opt. **27**, 663–665 (1988).
10. D. Casasent and D. Psaltis, "Scale-invariant optical correlation using Mellin transforms," Opt. Commun. **17**, 59–63 (1976).
11. D. Casasent and D. Psaltis, "Position, rotation, and scale invariant optical correlation," Appl. Opt. **15**, 1795–1799 (1976).
12. D. Casasent and D. Psaltis, "New optical transforms for pattern recognition," Proc. IEEE **65**, 77–84 (1977).
13. C.-Y. Lin, M. Wu, J. A. Bloom, I. J. Cox, M. L. Miller, and Y. M. Lui, "Rotation, scale and translation resilient watermarking for images," IEEE Trans. Image Process. **10**, 767–782 (2001).
14. J. Esteve-Taboada, J. García, and C. Ferreira, "Rotation-invariant optical recognition of three-dimensional objects," Appl. Opt. **39**, 5998–6005 (2000).
15. D. Sazbon, Z. Zalevsky, E. Rivlina, and D. Mendlovic, "Using Fourier-Mellin-based correlators and their fractional versions in navigational tasks," Pattern Recogn. **35**, 2993–2999 (2002).
16. D. Asselin and H. H. Arsenault, "Rotation and scale invariance with polar and log-polar coordinate transformation," Opt. Commun. **104**, 391–404 (1994).
17. J. Rosen and J. Shamir, "Scale invariant pattern recognition with logarithmic radial harmonic filter," Appl. Opt. **28**, 240–244 (1989).
18. Recall that a PMT image is plotted as a function of ρ and θ. In the θ direction, any image will cover the whole range from θ to 2π. As a result, two PMT images in two boxes adjacent in the vertical direction will tend to merge into each other. This problem is circumvented by scaling each PMT image to 90% of its actual size, thus creating a guard band. This step does not affect the outcome of the correlator process.